Noble metals-deposited TiO$_2$ photocatalysts for photoreduction of CO$_2$: Exploration of surface chemistry and a reflection on the importance of wavelength dependence

Mohit Yadav [a], Haythem S. Basheer [a], Ádám Ágfalvi [a], Kornélia B. Ábrahámné [a], Janos Kiss [a], Gyula Halasi [a,c], András Sápi [a,*], Ákos Kukovecz [a], Zoltán Kónya [a,b]

[a] *Department of Applied and Environmental Chemistry, Interdisciplinary Excellence Centre, University of Szeged, H-6720, Rerrich Bela ter 1, Szeged, Hungary*
[b] *ELKH-SZTE Reaction Kinetics and Surface Chemistry Research Group, University of Szeged, H-6720, Rerrich Bela ter 1, Szeged, Hungary*
[c] *ELI-ALPS, ELI-HU Non-Profit Ltd., H-6728, Wolfgang Sandner utca 3., Szeged, Hungary*

ARTICLE INFO

ABSTRACT

We report the enhanced photocatalytic performance of CO$_2$ reduction by introducing noble metal-deposited TiO$_2$ photocatalysts (NMD/TiO$_2$) under both visible light irradiation (VLI) and UV. It was found that NMD-TiO$_2$ samples demonstrated an expanded ability for light absorption, resulting in an improved photoefficiency for CO$_2$ reduction and selectivity towards carbon monoxide (CO). The conversion yields of CO$_2$ to CO followed the order: Rh >Ru >Pt and with Rh/TiO$_2$ reached 10.65 μmol/g$_{cat}$ (under visible light) and 7.84 μmol/g$_{cat}$ (under UV), which are ~3 and 10 times more as compared to pristine anatase TiO$_2$ (0, and 2.43 μmol/g$_{cat}$). Various factors were addressed including theoretical studies via DFT revealed that the formation of new impurity energy state levels in NMD/TiO$_2$, which act as acceptor levels. Moreover, DRIFTS studies showed that the H-O-C-O and formyl (H$_2$CO) species were the important intermediates towards the hydrogenation of CO$_2$ to CO. Also, a charge transfer mechanism toward CO$_2$ reduction was elucidated.

1. Introduction

Over the years, due to the buildup of greenhouse gases like CO$_2$ in significant proportions, the ecosystem has suffered. Therefore, it is imperative to apply an effective catalytic process that can convert CO$_2$ into value-added C1 compounds to reduce atmospheric CO$_2$ levels [1]. Among various techniques, catalytic CO$_2$ reduction with hydrogen as a reductant is one of the most extensively explored techniques, if an economically feasible and carbon-neutral supply of hydrogen can be developed. The reduction of CO$_2$ with hydrogen yields various important chemicals such as formic acid, ethanol, methanol, and vital other hydrocarbons [2,3]. The CO$_2$ conversion to value-added products is an effective one-step process, however, CO$_2$ is thermodynamically stable which makes it kinetically unreactive [4]. Reverse water gas shift reaction (RWGS) is a highly efficient strategy for CO$_2$ reduction into CO (RWGS: CO$_2$ + H$_2$ → CO + H$_2$O) [5]. In various well-established catalytic processes including Fischer–Tropsch (FT), CO is an important key intermediate in the manufacturing of value-added industrial chemicals [6]. Significant efforts have been undertaken to advance the

development of efficient heterogeneous catalysts and enhance high-temperature RWGS processes. As RWGS is an endothermic reaction that requires high temperature, which is mostly not feasible for future chemical plants where onsite/ distributed systems are desired. Thus, developing a catalyst that can operate at ambient temperature and pressure in RWGS is of vital importance.

Photocatalytic CO$_2$ reduction into reusable hydrocarbons under solar light as the photon source at ambient conditions can mimic the natural photosynthesis course [7,8]. There have been numerous reports related to TiO$_2$ on the photoreduction of CO$_2$ under light irradiation [9–12]. It is non-toxic, photostable, and reasonably cheap making it a suitable candidate for photocatalysis. However, it can only be stimulated by UV light (<400 nm), which makes up just 4 % of the solar spectrum, due to its broad band-gap value (~3.2 eV). Therefore, to efficiently exploit the solar light researchers across the globe worked extensively to modify TiO$_2$ for visible-light photocatalysis. In this regard, associating TiO$_2$ with noble metals is one of the key tactics to enhance VLD photocatalytic response [13–15]. The noble metal-loaded TiO$_2$ co-catalysts could efficiently trap the electrons, which can reduce the recombining tendency

of the photogenerated e⁻-h⁺ pairs for improved photocatalytic action. There have been reports including the noble metal-deposition on TiO_2 surface for CO_2 photoreduction [16,17]; on the contrary, the unloaded TiO_2 was inactive under the same reaction conditions [11,12,18]. Moreover, there have been studies in which usually only one metal was deposited as a co-catalyst, and many type of co-catalysts have not been thoroughly studied.

In the present study, we used Rh, Ru, and Pt nanoparticles deposited in 1 wt% on the TiO_2 surface as catalysts for the RWGS reaction at an ambient temperature and pressure. In addition, the photocatalytic efficacy was also compared under VLI and UV for all the samples. The noble metals exhibited a dual role as catalytic sites for CO generation and light harvesters injecting e⁻ into the conduction band of TiO_2. Moreover, we have also determined the reaction mechanism with the DRIFTS study, which created new opportunities for using this kind of catalyst in photocatalysis.

2. Experimental

2.1. Materials

Rhodium(III) chloride, Ruthenium(III) chloride, and chloroplatinic acid hexahydrate were procured from Sigma-Aldrich used as precursors for the synthesis of Ru, Rh, and Pt nanoparticles. Milli-Q water and absolute ethanol were used for washing and purification of the samples by centrifugation. A gas mixture of CO_2:H_2 = 1:2 ratios was used for the photocatalytic measurements. TiO_2 anatase (commercial), enamel grade was used as a reference sample.

2.2. Synthesis

The 1 wt% Rh/TiO_2 catalysts were synthesized by impregnating anataseTiO_2 powder (with a surface area of 48 m^2 g^{-1}) in an aqueous solution of $RhCl_3$ in an ultrasonic bath overnight, and dried in an oven at 80 °C. The obtained sample was calcinated at 350 °C in an oxidative and reductive environment for 2 h to get the Rh/TiO_2 catalyst. The Pt/TiO_2 and Ru/TiO_2 samples were prepared by using $H_2PtCl_6·6 H_2O$ and $RuCl_3$ as Pt and Ru precursors, respectively.

2.3. Characterization

A Rigaku Miniflex-II X-ray diffractometer with Ni-filtered Cu Kα radiation ($\lambda = 1.54$ Å) functioned at 15 mA and 30 kV was used to obtain XRD patterns. A FEI TECNAI G2 20 X-Twin high-resolution TEM was used to examine the morphological characterization of the samples. DRIFTS spectra of the samples were analysed on FTIR spectrometer (Agilent Cary-670) equipped with a diffuse reflectance attachment (Harrick Praying Mantis™). The sample holder consisted of two BaF_2 windows in the infrared path. Pre-treatment of the samples were same as described below in Section 2.4, and the background spectrum was recorded after cooled down to RT under helium flow. At RT, a CO_2:H_2 mixture (1:2) with a total flow rate of 15 mL·min⁻¹ was introduced into the DRIFTS cell followed by UV irradiation for 1, 5, 10, and 20 min. To avoid condensation, the tubes were externally heated. Typically, 32 scans were taken and all spectra were measured between 900 and 4000 cm⁻¹ at a resolution of 2 cm⁻¹. The contribution of the reactant gas mixture was observed to be negligibly small, because of the short optical path within the DRIFTS cell.

2.4. Photocatalytic CO_2 reduction experiment

Photocatalytic CO_2 reduction measurements were performed in a flow microreactor that comprised an inner glass (quartz) cylinder (h = 25 cm, diameter = 6.4 cm,) and an outer glass (quartz) cylinder (h = 25 cm, diameter = 10.2 cm). For the UV light source, a 11 W mercury vapor lamp (Heraeus Noblelight TQ 718, Hanau, Germany; λ_{max} = 254 nm)

was used. For visible light source, a 11 W LED (OSRAM DULUX D, $\lambda_{max} \geq$ 420 nm) was used. The irradiation intensity of the lamps on the photocatalytic surface was measured with a Quantum meter (Apogee, Model MQ-200), for visible lamp it was 283 μmol m^{-2} s^{-1} and for UV lamp it was 40 μmol m^{-2} s^{-1}, respectively. Initially, 250 mg of sample was ultrasonically dispersed in 10 mL of absolute ethanol, followed by immobilization on the exterior surface of the inner quartz cylinder. Then, the prepared catalysts film were pretreated with a heating rod at 250 °C with the introduction of various gases (i.e. (Ar for 20 min, O_2 for 30 min, Ar for 10 min, and H_2 for 60 min)) into the space between the cylinders. Then, CO_2:H_2 at a ratio of 1:2 as the reactant gas mixture was flowed with a mass flow controller (Aalborg) into the reactor. The fixed amount of reactant gas mixture was recirculated between the reactor and the gas chromatograph (GC) with a pump. A constant RT was maintained through the system during the measurements by recirculating cooling water. The identification and separation of the products and the reactants were carried out in an HP 5890 Series II GC equipped with a packed Porapak QS column (diameter = 0.635 cm, length = 2 m). The resulting products were identified with a thermal conductivity detector and flame ionization detector.

3. Results and discussion

3.1. Characterization

The phase purity and crystallographic structure of the as-prepared TiO_2, Rh/TiO_2, Ru/TiO_2, and Pt/TiO_2 samples were identified by the characteristic XRD patterns. As shown in Fig. 1(a), for pristine TiO_2 nanoparticles, the typical diffraction peaks at 25.27°, 36.95°, 37.84°, 38.61°, 48.11°, 53.97°, and 55.13° can be ascribed to the (101), (101), (004), (112), (200), (105) and (211) planes of cubic anatase (JCPDS NO-21–1272), respectively [14]. The noble metal-deposited TiO_2 samples showed a similar phase structure with higher dispersion, implying the introduction of noble metals into TiO_2 didn't alter any phase change. Primary crystallite sizes were calculated via the Scherrer formula, and the results are shown in Table 1. The sizes of the noble metal-containing samples remained almost the same in comparison with that of the TiO_2 sample.

The optical characteristics of the anatase and NMD/TiO_2 photocatalysts were scrutinized by DRS [Fig. 1(b)]. It can be witnessed that all the absorption spectra displayed a strong absorption band with a sharp edge, which is typical characteristic of wide-bandgap oxide semiconductors. Pristine TiO_2 showed high absorption at shorter wavelengths (<400 nm), which could be accredited to its intrinsic band gap absorption [19]. The noble metal-deposited TiO_2 samples were of grey color and showed enhanced absorption with a slight redshift in light response in comparison to pristine TiO_2. In addition, a hump (marked in green area) in the visible region with a shoulder band around 440–470 nm for Rh and Ru was observed Fig. 1(c), displaying surface plasmon resonance (SPR) owing to the free electron's collective oscillation in the conduction band [20]. However, Pt no plasmonic bands were observed due to the damping effect of d-d transition, which results in fewer contribution of free e⁻ to dielectric function [21]. The band gaps were estimated via the Kubelka-Munk equation (Table 1). Overall, the addition of noble metal slightly influenced the band gaps. Also, to our observations on primary crystallite size, no notable trend could be witnessed in the change of specific surface area (SSAs) for the NMD/TiO_2 samples (Table 1). TEM study was carried out to investigate the morphology and the presence of noble metal-deposition on TiO_2 surface (Fig. 2). The TEM micrograph of pristine anatase exhibit cubic-like morphology with an average diameter of about 30–70 nm. For NMD/TiO_2 samples, the noble metals seem to be uniformly incorporated on the TiO_2 surface.
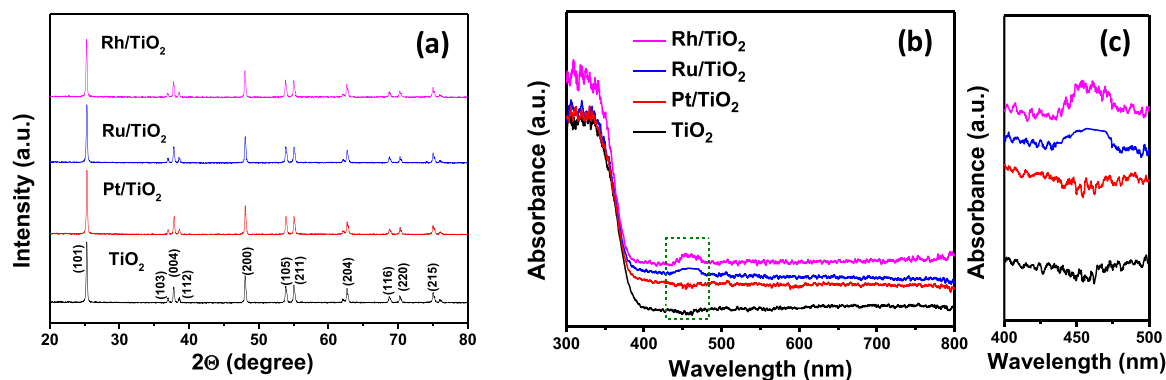
Fig. 1. (a) XRD patterns and (b) DRS of TiO_2 and NMD/TiO_2 photocatalysts, (c) Enlarged DRS of TiO_2 and NMD/TiO_2 samples.

Table 1
Catalyst loadings, band gaps, primary crystallite size, and BET surface areas.

Sample	Rh, Ru and Pt (wt%)	SSAs ($m^2 \cdot g^{-1}$)	Band gap (eV)	Primary crystallite size (nm)
TiO_2	–	48.8	3.28	19.31
Pt/TiO_2	1	48.9	3.24	19.43
Ru/TiO_2	1	49.1	3.22	19.39
Rh/TiO_2	1	49.4	3.16	19.35

3.2. Photocatalytic results

The photocatalytic CO_2 reduction experiments were executed to evaluate the photoactivity of the samples under UV and VLI at ambient conditions. Initially, control experiments were conducted (Fig. 3a), and it was observed that the catalysts were inactive in the dark. However, after UV-light irradiation, pristine TiO_2 showed little photoreduction activity and was highly selective towards CO formation. The noble metal-deposited TiO_2 samples showed much-enhanced photoreduction efficiency towards CO_2 following the order Rh > Ru > Pt. Under VLI (Fig. 3b), the photoefficacy of the NMD/TiO_2 samples further increased as compared to the UV-light irradiation. As expected the bare TiO_2 displayed poor photoreduction efficiency towards CO_2, and Rh/TiO_2 sample showed the highest photoactivity activity along with a higher CO yield (Fig. 3c), which turned out be almost ~3 times greater to its pure counterpart. Thus, the deposition of noble metal nanoparticles on the TiO_2 surface improved the formation yield of CO. The interaction between noble metal nanoparticles deposited on the surface of TiO_2 and adsorbed hydrogen is indeed crucial towards the higher CO yield. As the noble metal nanoparticles with a higher affinity for hydrogen can hold on to hydrogen more strongly, thereby; promoting its availability for RWGS. Therefore, it impacted the overall photocatalytic activity of the metal nanoparticle towards the higher CO formation rate as compared to pristine TiO_2 [22]. Interestingly, all the samples were highly selective towards CO yield with both UV and VLI (Fig. S1). To have in-depth understanding the basicity of the photocatalysts towards CO_2 adsorption, the total surface basicity of the Rh/TiO_2 sample along with pristine anatase were measured by CO_2-TPD, respectively. The characteristic CO_2-TPD profiles for the samples in the temperature range (100–500 °C)
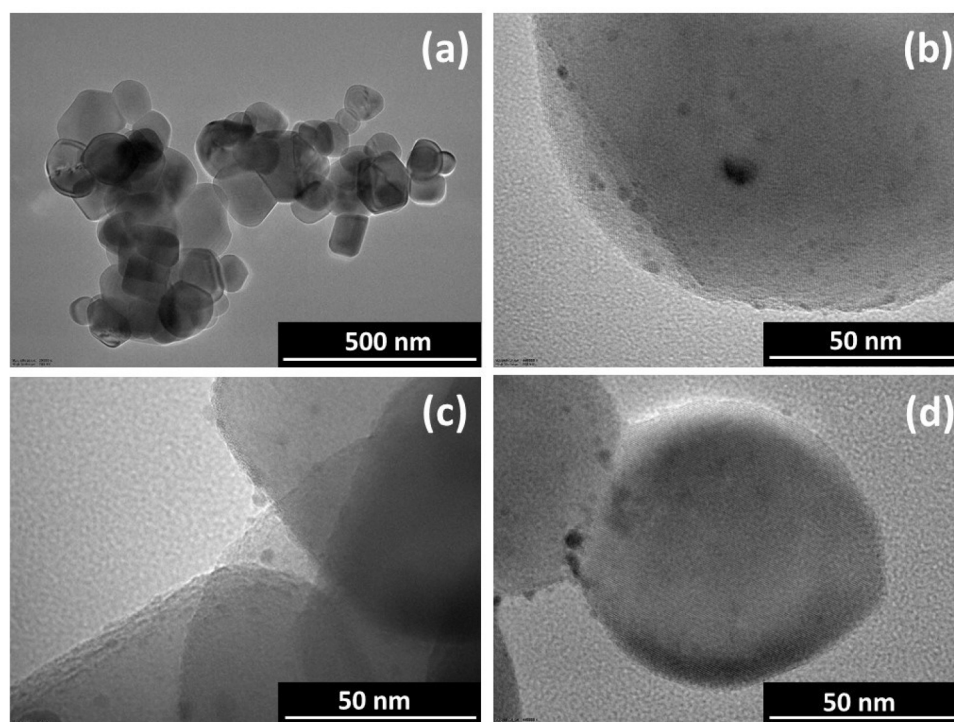
Fig. 2. TEM images of (a) TiO_2, (b) Pt/TiO_2, (c) Ru/TiO_2, and (d) Rh/TiO_2.
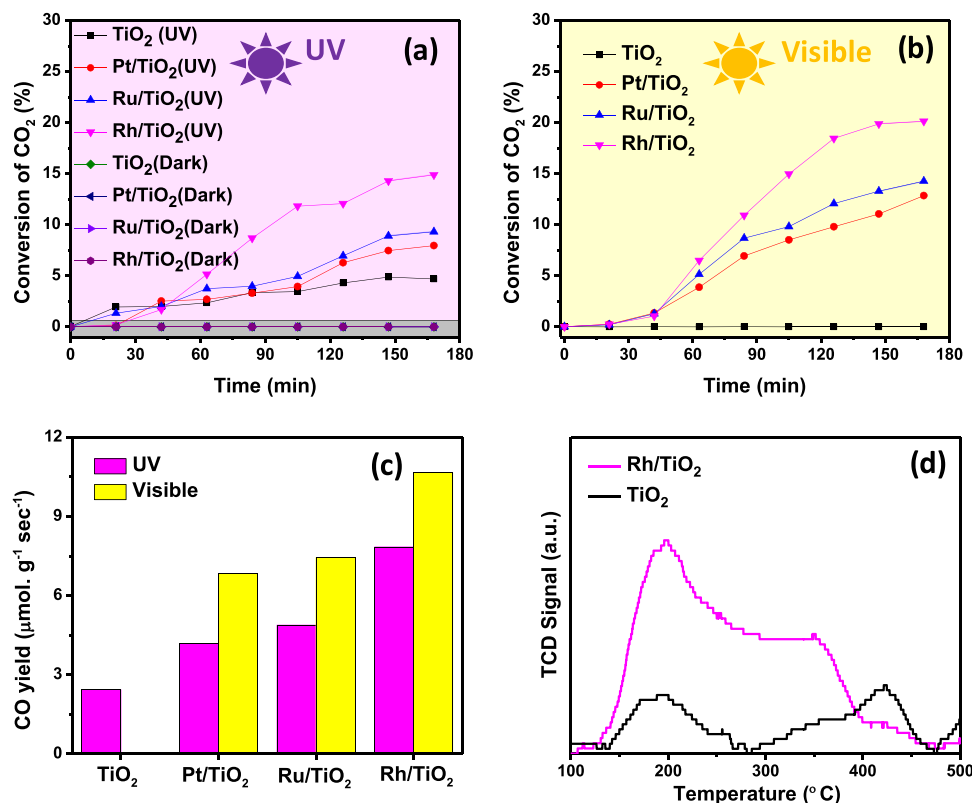
Fig. 3. Conversion of CO_2 under (a) UV light, (b) visible light, (c) CO Yield with TiO_2, Pt/ TiO_2, Ru/ TiO_2 and Rh/ TiO_2 photocatalysts under UV and Visible light irradiation. (d) CO_2-TPD profiles of the pristine TiO_2 and Rh/TiO_2 samples.

are showed in Fig. 3(d), which revealed that the Rh/TiO_2 had a very strong basicity with a much higher CO_2 desorption peak in comparison to pristine anatase. However, a negligible shift was observed in the CO_2 desorption peak for the Rh/TiO_2 sample from 197.8 °C to 198.1 °C, but the amount of desorbed CO_2 improved by almost 3.5 times from 0.004 to 0.014 mmol g^{-1} (Table 2). Overall, the Rh/TiO_2 sample had a larger number of basic sites. Consequently, the deposition of Rh seemingly led to produce more active centers toward CO_2 adsorption. In addition, the enhanced photoreduction efficiency of NMD-TiO_2 samples can also be accounted for by the strong Schottky barrier that formed at the noble metals and TiO_2 interface, which efficiently trapped e^- and inhibited e^--h^+ recombination [20].

The NMD-TiO_2 samples showed a conspicuous higher photocatalytic activity under VLI as compared with UV-light owing to a distinct light response mechanism. Firstly, we noticed that the optical light response of the NMD-TiO_2 samples was enhanced and the band gap values were slightly decreased leading to a higher formation of photogenerated charge carriers. The noble metals Nps deposited on the TiO_2 surface exhibited SPR that could potentially absorb visible, allowing them to

harvest a broader range of the solar spectrum. This increased light absorption resulted in more efficient utilization of sunlight for photocatalytic reactions. In addition, noble metal Nps could generate hot electrons with higher kinetic energy, which can be effectively transferred to the TiO_2 semiconductor, they could generate additional electron-hole pairs, leading to enhanced photocatalytic activity [23]. Also, bare TiO_2 possesses a rich defect chemistry that can directly influence its photoresponse characteristics [24–26]. TiO_2 in its Ti^{3+} defect state is the most prominent defect positioned just under the CBM inflicting high UV photoresponse owing to an effectual transfer of e^- through the defect sites. However, under VL, it reaches the maximum level due to the cumulative effect from Rh Nps and anatase. In the case of anatase, the photoresponse towards VL is not significant compared to its UV photoresponse.

3.3. DRIFTS and photocatalytic mechanism

To interpret the reaction pathway of photocatalytic CO_2 hydrogenation, in-situ DRIFTS characterization was performed. The pristine TiO_2 showed a little photoreduction activity and was highly selective towards CO formation. Rh, Ru and Pt deposition increased the photoactivity. The DRIFTS feature showed the similar reaction mechanism, namely the CO_2 reduction proceeds via RWGS mechanism [27]. Both theoretically and experimentally proved that H_2 dissociation on the Pt metal nanoparticles is not problematic under CO_2 hydrogenation conditions. Previous experimental and theoretical studies showed H_2 dissociation on Pt metals occurred at much lower temperatures than that for CO_2 hydrogenation [28]. The Rh/TiO_2 was the most active photocatalyst and the observed DRIFTS feature during the reaction, differs a little bit from the other two catalysts, we demonstrate detail spectra from Rh/TiO_2 [(Fig. 4(a). No formate formation, as an intermediate was observed which is frequently found in photochemical reduction of CO_2 [29,30]. Between 3600 and 3800 cm^{-1} two doublet (not shown)

Table 2
Conversion of CO_2, yield of CO obtained with TiO_2 and NMD/TiO_2 photocatalysts under UV and Visible light irradiation, and CO_2-TPD results for pristine TiO_2 and Rh/TiO_2 samples.

Samples	CO_2 conversion (%)		CO Yield ($\mu mol \cdot g^{-1} \cdot sec^{-1}$)		Desorption Temperature (°C)	Basicity by strength (mmol g^{-1})
	UV	Visible	UV	Visible		
TiO_2	4.6	0.0	2.43	0.0	197.8	0.004
Pt/TiO_2	7.9	12.9	4.18	6.84	–	–
Ru/ TiO_2	9.3	14.2	4.88	7.44	–	–
Rh/ TiO_2	14.8	20.1	7.84	10.65	198.1	0.014

was detected and can be ascribed to the combined tones of adsorbed CO_2 molecules [31]. It seems that the dominant adsorption species are the different adsorption forms of CO. In the first steps the photoactivated negatively charged CO_2 decomposes to adsorbed CO which remains adsorbed state or leave the surface as a reaction product. The transiently formed H-O-C-O intermediate has a short lifetime and reacts further:

$$CO_2 + h\nu \rightarrow CO_2^-(a) \tag{1}$$

$$CO_2^-(a) \rightarrow CO(a) + O(a) \tag{2}$$

$$CO_2^- + H(a) \rightarrow H\text{-}O\text{-}C\text{-}O(a) \tag{3}$$

$$H\text{-}O\text{-}C\text{-}O(a) \rightarrow CO(a) + OH(a) \tag{4}$$

The band at 2077 cm^{-1} is accredited to the linearly bonded adsorbed CO [32] which was detected all three catalysts. The band at 2025 cm^{-1} on Rh/TiO_2 is also adsorbed CO related band. The band observed during the reaction at 2025 cm^{-1} on Rh/TiO_2 can be attributed to CO perturbed by hydrogen (HCO) [33]. The hydrogen assisted CO was found earlier during $CO\text{-}H_2$ coadsorption on noble metals. This coadsorbed intermediate can be ascribed with a twin structure where one hydrogen and one CO bond to the same Rh site [34]. We may suggest that this kind of adsorbed CO is influenced by hydrogen:

$$CO(a) + H(a) \rightarrow HCO(a) \tag{5}$$

$$HCO(a) + H(a) \rightarrow H_2CO(a) \tag{6}$$

Morever, on Rh/TiO_2 an intense band at 1785 cm^{-1} was produced during extensive irradiation and it can be attributed to the formation of formyl species (H_2CO) which was found earlier during CO_2 reduction on several metal deposited catalysts [35,28,36]. This infrared band was

observed during formaldehyde adsorption and reaction on Rh/TiO_2 assigned to formyl species [37]. The existence of formyl is gained the band developed parallel at 2808 cm^{-1} attributed to C-H mode for formyl. Formyl species can easily form hydrogen perturbed CO surface intermediate (step 5,6). We may assume that step (7) and perhaps (6) could be photo initiated processes and it can be an extra source for CO production. This CO evolution may contribute to the increase of activity of Rh/TiO_2 catalysts.

$$CH_2O(a) + h\nu \rightarrow CO(a)(g) + H_2(g) \tag{7}$$

Fig. 4(b) compares the PL spectra for TiO_2 with the NMD/TiO_2 samples. Clearly, the NMD/TiO_2 photocatalysts showed a PL signal similar to the curve shape of anatase, however, PL intensity of the NMD/TiO_2 samples was reduced substantially as compared to their counterpart, thereby; signifying the presence of noble metals influenced the PL phenomenon. In addition, the NMD/TiO_2 displayed strong and wide PL signals ranging from 450 to 480 nm with an exciting wavelength of 370 nm. For pristine anatase the spectral peak was located at 457 nm. The suppressed PL intensity for NMD/TiO_2 samples is perhaps due to the deposition onto the TiO_2 surface. Thus, in the case of NMD/TiO_2 samples, the $e^-\text{-}h^+$ pairs recombination rate was successfully inhibited, which led to the higher photocatalytic efficiency towards CO_2 reduction as compared to pristine TiO_2 under both UV and VLI [2]. In addition, a photocatalytic mechanism was interpreted for the CO_2 reduction with Rh/TiO_2 to understand the charge transfer mechanism. Therefore, the VBM and CBM potentials of the pristine anatase can be measured using Eqs. (6) and (7) [38]:

$$E_{CB} = X - E^e - 0 \cdot 5E_g \tag{8}$$
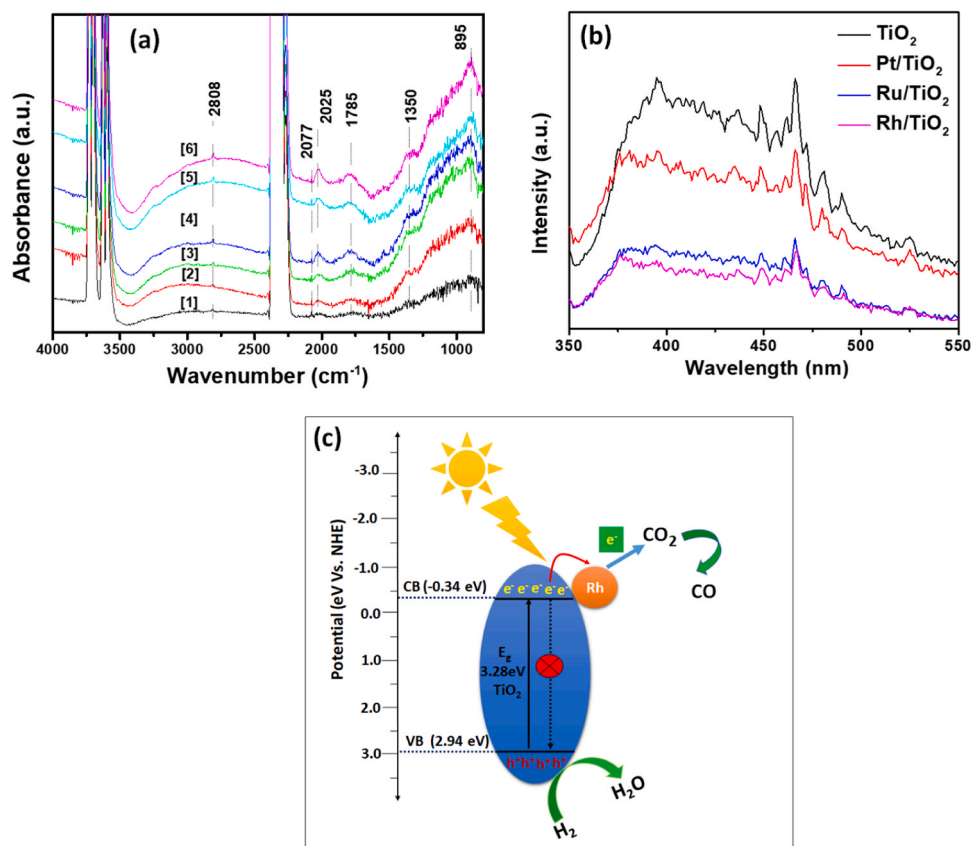
$$E_{VB} = E_{CB} + E_g \tag{9}$$

Fig. 4. (a) DRIFTS spectra of Rh/TiO_2 sample. The numbers in the last three figures represent the following: (1) at RT for 20 min, (2) at RT for 20 min + under UV exposure for 5 min, (3) at RT for 20 min + under UV exposure for 10 min, and (4) at RT for 20 min + under UV exposure for 20 min (b) PL spectra of the anatase and NMD/TiO_2 samples. (c) Probable photocatalytic mechanism of CO_2 reduction over Rh/TiO_2 sample.

where X represents the TiO$_2$'s absolute electronegativity that can be defined as the arithmetic mean of the first ionization of the constituent atoms and electron affinity. The X was determined to be 5.8 eV as per literature [39,40], E$_g$ is the bandgap energy of TiO$_2$ (3.28 eV), and on the hydrogen scale, E^e is the free electrons energy i.e. 4.5 eV. Consequently, the VBM and CBM of TiO$_2$ vs. normal hydrogen electrode (NHE) were determined (E$_{CB}$ = –0.34 V and E$_{VB}$ = +2.94 V). Based on overall results, the photocatalytic CO$_2$ reduction mechanism with H$_2$ over Rh/TiO$_2$ is showed in Fig. 4(c). The Rh Nps are well immobilized at the anatase's surface. Rh being a noble metals being a good conductor can actively contribute in photoelectron interaction with the adsorbed CO$_2$ at the catalyst's surface [33]. Consequently, the deposited Rh TiO$_2$'s surface interface enriches the charge parting and constrains the recombining tendency of the photogenerated e$^-$-h$^+$ pairs due to the formation of Schottky barriers [41]. Thus, Rh metal ions with plenty of electrons efficiently lead to the CO$_2$ reduction. Meanwhile, the VB potential of TiO$_2$ with the photogenerated h$^+$ reacts with H$_2$ to produce H$_2$O in small amounts as the byproducts [42–44].

3.4. First principles calculations based on density functional

The measured band-gap of NMD-TiO$_2$ samples was observed to be influential on the photocatalytic activity and the relative energy change was considered. In this calculation, a single unit cell of the bulk decorated with one atom Fig. (5) using quantum espresso burai which is a part of quantum espresso open-source suite software from quantum simulation of materials first the systems. the spin-polarized density functional theory (DFT) was analyzed by means of general gradient approximation (GGA) plus U with U values 5 eV and 500 eV for energy cutoff [45,46]. To investigate the relative change in energies of the NMD-TiO$_2$ samples. The band gap of pure anatase was found to be 3.28 eV the value of the band gap is consistent with the previous results [47]. The Fermi level is in between the energy VB and the CB from –1.4–1.5 eV this is owing to the contribution of O 2p orbitals and Ti orbitals hybridization. The bandgap of NMD-TiO$_2$ samples decreased slightly and it was found to be 1.6, 0.9, and 0.5 eV for Pt, Ru and Rh atoms deposited on TiO$_2$ can reduce the band respectively (Fig. S2). Moreover, in this case, Rh/TiO$_2$ has the narrowest band gap this may be to the small system model, most of the transition metal reducing the band gap [48,49]. The band structure of Rh/TiO$_2$ [Fig. S2(g)] shows the overlap of the valence bands with conductive bands. The total partial

density of states (TPDOS) of Pt, Ru, and Rh decorated anatase TiO$_2$ bulk displayed in Fig. 6(b, c, and d). The DOS shape of the decorated anatase showed some broading compared to the pure anatase, which reveals that the electronic nonlocalized bands is clear as the result of hybridization figure 7 (d, f and h). DOS Pt/TiO$_2$ in Fig. (6) shows the decorated Pt on the surface of anatase Pt-Ti interact hybridized peak at the top of the CB.

For Ru/TiO$_2$ PDOS calculation agreeing to Ru 3d shows some new energy level band located above the top VB. PDOS in Fig. (6) reveals that Ru 3d has as an isolated energy level located slightly at the bottom of the CB with completely occupied and the other one is unoccupied. This energy level is sufficient to overlap and minimize the TiO$_2$ surface energy levels. The PDOS Fig. 6(d) for Rh/TiO$_2$ shows the new impurity state completely fills most of the CB and VB space and the band gap is reduced almost to zero which acts like metals this may be due to small the model system used which consist of one anatase unit cell and one Rh atom.

Fig. 6(b, c and d) show the calculated partial density of state for Pt, Ru and Rh decorated anatase systems. The valence band of the pure bulk anatase surface is located between –1.4 eV and –6.8 eV mainly generated by O 2p states, which are intershell electrons. The Fermi level is located in the middle of CB and VB, which are mainly formed by O 2p state levels and Ti 3d states and O 2p is dominating the energy level states and then Ti 3d states. It's appeared that the CB of Pt/TiO$_2$, Ru/TiO$_2$, and Rh/TiO$_2$ are composed only of Ti and Pt, Ru and Rh states mainly while VB mainly composed of O states. In the systems, the new energy level is localized above the top of the VB of the hybrid O 2p, Ti3d, and (Pt 3d, Ru 3d, and Rh 3d) states. In conclusion, the loading of Pt, Ru, and Rh reduced the band gap and form new state levels these impurity energy state levels, act as acceptor levels that suppress the recombining rate of the e$^-$-h$^+$ pairs as a result photoactivity can be improved. Moreover, a comparison is drawn with the efficiency of the Rh/TiO$_2$ sample with some of the previously reported photocatalysts towards photocatalytic CO$_2$ hydrogenation, which can be seen in Table 3. Noticeably, the Rh/TiO$_2$ sample seems to be comparable with previously reported materials towards RWGS in terms of higher CO yield.

4. Conclusions

In summary, the noble metals were deposited on the anatase TiO$_2$ surface via the wet impregnation route. The light absorption characteristics of the NMD-TiO$_2$ photocatalysts were positively influenced,
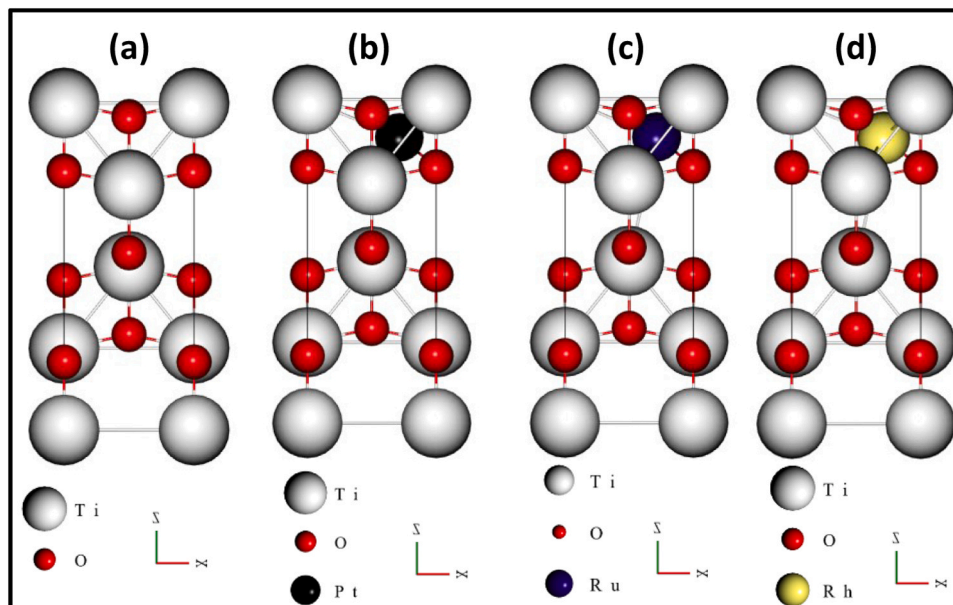
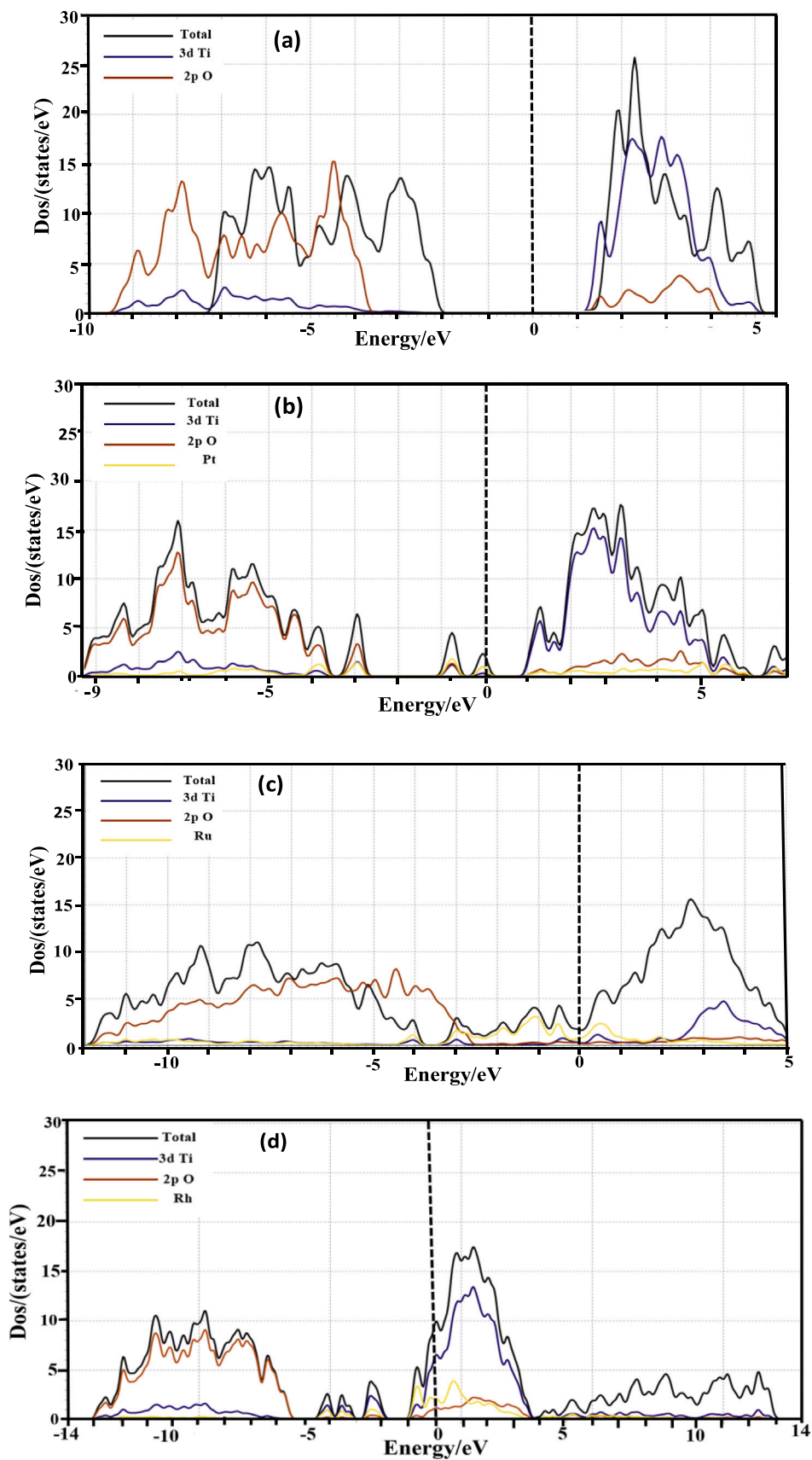**Fig. 5.** The model structure of (a) TiO$_2$, (b), Pt/TiO$_2$, (c), Ru/TiO$_2$, and (d) Rh/TiO$_2$.

Fig. 6. TPDOS for (a) TiO_2, (b) Pt/TiO_2, (c) Ru/TiO_2, and (d) Rh/TiO_2.

Table 3

Comparison Rh/TiO$_2$ sample with the previous literature towards photocatalytic CO$_2$ reduction under certain reaction conditions.

Photocatalyst	Reaction condition	CO yield (μmol g^{-1} h^{-1})	References
Pt/TiO$_2$ 5 h	400 W Xe lamp 19.6 mW/ cm^2 (Intensity) UV(250–388 nm), 298 K and 2 atm	179.34	[50]
1 wt% Pt/ TiO$_2$	400–510 nm visible light 450 nm (Intensity), 293 K	4.2	[51]
PtTiO$_{2-x}$	450 W Xe lamp visible light, 150°C	27	[52]
0.5 % Pt/TiO$_2$	400 W Hg Lamp, 450°C	2.5	[53]
Ru/TiO$_2$	UV irradiation + 200°C	153	[54]
Rh(1)TiO$_2$	500 W mercury lamp, 673 K	9.2	[41]
Pt/TiO$_2$(G)	UV irradiation, 400°C	63.3	[55]
Pt/TiO2	254 nm UV-A irradiation, 80°C	0.067	[14]
Rh/TiO$_2$	300 W Xe light, 500°C	0.144	[56]
1 % Ru- TiO$_{2-x}$	300 W xenon lamp, 160°C	7.3	[57]
Rh/TiO$_2$	**UV and Visible-light-irradiation**	**10.65**	**Present work**

which allowed the Rh Nps to absorb photons and inject e$^-$ into the CB of the anatase. Rh/TiO$_2$ showed the highest conversion of CO$_2$ among the NMD-TiO$_2$ samples along with a high yield of CO under both UV and VLI. The deposition of noble metals on anatase generated new impurity energy state levels, which act as acceptor levels as depicted by DFT calculations. Moreover, the H-O-C-O and formyl (H$_2$CO) species were the important intermediates towards the reduction of CO$_2$ to CO. The recombining ability of the photogenerated e$^-$-h$^+$ pairs was successfully inhibited which facilitated the charge transfer mechanism toward CO$_2$ reduction.

CRediT authorship contribution statement

Mohit Yadav: Conceptualization, Software, Validation, Formal analysis, Investigation, Writing - Original Draft, Data Curation, Methodology, Visualization. **Haythem S Basheer:** Software, Investigation, Data Curation. **Ádám Ágfalvi:** Conceptualization, Formal analysis, Investigation. **Kornélia B Ábrahámné :** Resources, Investigation. **Janos Kiss:** Software, Formal analysis, Resources. **Gyula Halasi:** Software, Formal analysis, Resources. **András Sápi:** Conceptualization, Software, Validation, Data Curation, Methodology, Resources, Visualization, Supervision, Project administration, Funding acquisition. **Ákos Kukovecz:** Resources, Visualization, Supervision, Project administration, Funding acquisition. **Zoltán Kónya:** Resources, Visualization, Supervision, Project administration, Funding acquisition.

Declaration of Competing Interest

The authors declare that they have no known competing financial interests or personal relationships that could have appeared to influence the work reported in this paper.

Data Availability

Data will be made available on request.

Acknowledgements

Appendix A. Supporting information

Supplementary data associated with this article can be found in the online version at doi:10.1016/j.apcata.2023.119434.

References

[1] A. Jangam, S. Das, N. Dewangan, P. Hongmanorom, W.M. Hui, S. Kawi, Catal. Today 358 (2020) 3–29.
[2] M. Tahir, N.S. Amin, Appl. Catal. B: Environ. 162 (2015) 98–109.
[3] P. Li, L. Liu, W. An, H. Wang, H. Guo, Y. Liang, W. Cui, Appl. Catal. B: Environ. 266 (2020), 118618.
[4] F. Zhang, Y.-H. Li, M.-Y. Qi, Y.M. Yamada, M. Anpo, Z.-R. Tang, Y.-J. Xu, Chem. Catal. 1 (2021) 272–297.
[5] Q. Zhang, M. Bown, L. Pastor-Pérez, M.S. Duyar, T.R. Reina, Ind. Eng. Chem. Res. 61 (2022) 12857–12865.
[6] Z. Teimouri, V.B. Borugadda, A.K. Dalai, N. Abatzoglou, Renew. Sustain. Energy Rev. 160 (2022), 112287.
[7] D. Qin, Y. Zhou, W. Wang, C. Zhang, G. Zeng, D. Huang, L. Wang, H. Wang, Y. Yang, L. Lei, J. Mater. Chem. A 8 (2020) 19156–19195.
[8] X. Ren, M. Gao, Y. Zhang, Z. Zhang, X. Cao, B. Wang, X. Wang, Appl. Catal. B: Environ. 274 (2020), 119063.
[9] S.N. Habisreutinger, L. Schmidt-Mende, J.K. Stolarczyk, Angew. Chem. Int. Ed. 52 (2013) 7372–7408.
[10] K. Kočí, L. Obalová, Z. Lacný, Chem. Pap. 62 (2008) 1–9.
[11] T. Mizuno, K. Adachi, K. Ohta, A. Saji, J. Photochem. Photobiol. A: Chem. 98 (1996) 87–90.
[12] S. Kaneco, H. Kurimoto, K. Ohta, T. Mizuno, A. Saji, J. Photochem. Photobiol. A: Chem. 109 (1997) 59–63.
[13] A.P. Manuel, K. Shankar, Nanomaterials 11 (2021) 1249.
[14] N. Singhal, U. Kumar, Mol. Catal. 439 (2017) 91–99.
[15] D. Lan, F. Pang, J. Ge, ACS Appl. Energy Mater. 4 (2021) 6324–6332.
[16] H. Abdullah, M.M.R. Khan, H.R. Ong, Z. Yaakob, J. CO₂ Util. 22 (2017) 15–32.
[17] A. Larimi, M. Rahimi, F. Khorasheh, Renew. Energy 145 (2020) 1862–1869.
[18] S. Kaneco, H. Kurimoto, Y. Shimizu, K. Ohta, T. Mizuno, Energy 24 (1999) 21–30.
[19] Y. Yang, L.C. Yin, Y. Gong, P. Niu, J.Q. Wang, L. Gu, X. Chen, G. Liu, L. Wang, H. M. Cheng, Adv. Mater. 30 (2018), 1704479.
[20] C. Wang, S. Fang, S. Xie, Y. Zheng, Y.H. Hu, J. Mater. Chem. A 8 (2020) 7390–7394.
[21] A. Wood, M. Giersig, P. Mulvaney, J. Phys. Chem. B 105 (2001) 8810–8815.
[22] D. McKee, J. Catal. 8 (1967) 240–249.
[23] F. Wang, R.J. Wong, J.H. Ho, Y. Jiang, R. Amal, ACS Appl. Mater. Interfaces 9 (2017) 30575–30582.
[24] R. Liu, P. Wang, X. Wang, H. Yu, J. Yu, J. Phys. Chem. C 116 (2012) 17721–17728.
[25] U. Diebold, Surf. Sci. Rep. 48 (2003) 53–229.
[26] M.A. Henderson, Surf. Sci. Rep. 66 (2011) 185–297.
[27] S. Kattel, B. Yan, J.G. Chen, P. Liu, J. Catal. 343 (2016) 115–126.
[28] A. Sápi, G. Halasi, J. Kiss, D.G. Dobó, K.L. Juhász, V.J. Kolcsár, Z. Ferencz, G. Vári, V. Matolin, As Erdőhelyi, J. Phys. Chem. C 122 (2018) 5553–5565.
[29] B. László, K. Baán, E. Varga, A. Oszkó, A. Erdőhelyi, Z. Kónya, J. Kiss, Appl. Catal. B: Environ. 199 (2016) 473–484.
[30] J. Kiss, Á. Kukovecz, Z. Kónya, Catal. Lett. 149 (2019) 1441–1454.
[31] J. Wu, C.-W. Huang, Front. Chem. Eng. China 4 (2010) 120–126.
[32] J. Kiss, F. Solymosi, J. Catal. 179 (1998) 277–282.
[33] J. Zheng, P.R. Nicovich, R.M. Dickson, Annu. Rev. Phys. Chem. 58 (2007) 409.
[34] A.M. Abdel-Mageed, D. Widmann, S.E. Olesen, I. Chorkendorff, R.Jr Behm, ACS Catal. 8 (2018) 5399–5414.
[35] Y. Guo, S. Mei, K. Yuan, D.-J. Wang, H.-C. Liu, C.-H. Yan, Y.-W. Zhang, ACS Catal. 8 (2018) 6203–6215.
[36] A. Sápi, R. Thangavel, M. Yadav, J. Kiss, Á. Kukovecz, Z. Kónya, Springer 2022, pp. 605–646.
[37] J. Raskó, T. Kecskés, J. Kiss, J. Catal. 226 (2004) 183–191.
[38] S.R. Morrison, S. Morrison, Springer 1980.
[39] T. Xian, H. Yang, L. Di, J. Ma, H. Zhang, J. Dai, Nanoscale Res. Lett. 9 (2014) 1–9.
[40] J. Lu, H. Jin, Y. Dai, K. Yang, B. Huang, Int. J. Photo 2012 (2011).
[41] Y. Kohno, Y. Hayashi, S. Takenaka, T. Tanaka, T. Funabiki, S. Yoshida, J. Photochem. Photobiol. A: Chem. 126 (1999) 117–123.
[42] J. Rasko, F. Solymosi, J. Phys. Chem. 98 (1994) 7147–7152.
[43] B. Pan, Y. Wu, B. Rhimi, J. Qin, Y. Huang, M. Yuan, C. Wang, J. Energy Chem. 57 (2021) 1–9.

[44] J. Zhao, Y. Wang, Y. Li, X. Yue, C. Wang, Catal. Sci. Technol. 6 (2016) 7967–7975.

[45] J.P. Perdew, K. Burke, M. Ernzerhof, Phys. Rev. Lett. 77 (1996) 3865.

[46] P. Giannozzi, S. Baroni, N. Bonini, M. Calandra, R. Car, C. Cavazzoni, D. Ceresoli, G.L. Chiarotti, M. Cococcioni, I. Dabo, J. Phys.: Cond. Matt. 21 (2009), 395502.

[47] J. Yu, P. Zhou, Q. Li, Phys. Chem. Chem. Phys. 15 (2013) 12040–12047.

[48] W.-K. Wang, J.-J. Chen, W.-W. Li, D.-N. Pei, X. Zhang, H.-Q. Yu, ACS Appl. Mater. Interfaces 7 (2015) 20349–20359.

[49] C. Jin, Y. Dai, W. Wei, X. Ma, M. Li, B. Huang, Appl. Surf. Sci. 426 (2017) 639–646.

[50] W.-N. Wang, W.-J. An, B. Ramalingam, S. Mukherjee, D.M. Niedzwiedzki, S. Gangopadhyay, P. Biswas, J. Am. Chem. Soc. 134 (2012) 11276–11281.

[51] D. Markovskaya, M. Lyulyukin, A. Zhurenok, E. Kozlova, Kin. Catal. 62 (2021) 488–495.

[52] Y. Wang, Q. Lai, Y. He, M. Fan, Catal. Commun. 108 (2018) 98–102.

[53] (a) N. Roy, Y. Sohn, D. Pradhan, ACS Nano 7 (2013) 2532–2540;
(b) L. Liu, Y. Jiang, H. Zhao, J. Chen, J. Cheng, K. Yang, Y. Li, ACS Catal. 6 (2016) 1097–1108.

[54] Y. Li, R. Li, Z. Li, Y. Xu, H. Yuan, S. Ouyang, T. Zhang, Sol. RRL 6 (2022), 2200493.

[55] P. Ebrahimi, A. Kumar, M. Khraisheh, Catalysis 12 (2022) 1101.

[56] C.-W. Lee, R.A. Kourounioti, J.C. Wu, E. Murchie, M. Maroto-Valer, O.E. Jensen, C.-W. Huang, A. Ruban, J. CO_2 Util. 5 (2014) 33–40.

[57] Y. Zhou, Q. Zhang, X. Shi, Q. Song, C. Zhou, D. Jiang, J. Colloid Interface Sci. 608 (2022) 2809–2819.